



Optical Transient Source AT2021lfa: A Possible “Dirty Fireball”

Xue-Mei Ye^{1,2}, Da-Ming Wei^{1,2}, Yi-Ming Zhu^{3,4} , and Zhi-Ping Jin^{1,2}

¹ Key Laboratory of Dark Matter and Space Astronomy, Purple Mountain Observatory, Chinese Academy of Sciences, Nanjing 210023, China; dmwei@pmo.ac.cn

² School of Astronomy and Space Science, University of Science and Technology of China, Hefei 230026, China

³ National Astronomical Observatories/Nanjing Institute of Astronomical Optics & Technology, Chinese Academy of Sciences, Nanjing 210042, China

⁴ CAS Key Laboratory of Astronomical Optics & Technology, Nanjing Institute of Astronomical Optics & Technology, Nanjing 210042, China

Received 2023 December 21; revised 2024 February 4; accepted 2024 February 18; published 2024 March 27

Abstract

AT2021lfa, also known as ZTF21aayokph, was detected by the Zwicky Transient Facility on 2021 May 4, at 05:34:48 UTC. Follow-up observations were conducted using a range of ground-based optical telescopes, as well as Swift/XRT and VLA instruments. AT2021lfa is classified as an “orphan afterglow” candidate due to its rapid flux decline and its reddened color ($g - r = 0.17 \pm 0.14$ mag). For an optical transient source without prompt gamma-ray detection, one key point is to determine its burst time. Here we measure the burst time through fitting the initial bump feature of AT2021lfa and obtain its burst time as 2021 May 3, at 22:09:50 UTC. Using `afterglowpy`, we model the multi-band afterglow of AT2021lfa and find that the standard model cannot reproduce the late radio observations well. Considering that the microphysical parameters ϵ_e , ϵ_B (the energy fraction given to electrons and magnetic field), and ξ_N (the fraction of accelerated electrons) may vary with time, we then model the afterglow of AT2021lfa taking into account the temporal evolution of the physical parameters ϵ_e , ϵ_B , and ξ_N and find in this case the multi-wavelength observations can be reproduced well. The initial Lorentz factor of AT2021lfa can be estimated from the peak time of the early afterglow, which yields a value of about 18, suggesting that AT2021lfa should be classified as a “dirty fireball.” From the upper limit for the prompt emission energy of AT2021lfa, we obtain that the radiation efficiency is less than 0.02%, which is much smaller than that of ordinary gamma-ray bursts (GRBs). It is also interesting that the fitted values of jet angle and viewing angle are very large, $\theta_c \sim 0.66$ rad, $\theta_v \sim 0.53$ rad, which may lead to the low Lorentz factor and radiation efficiency. When compared with GRB afterglow samples, it is evident that the onset bump timescale of AT2021lfa satisfies the empirical relationships observed in GRB samples. Additionally, the luminosity of AT2021lfa falls within the range of observations for GRB samples; however, approximately 1 day after the burst, its luminosity exceeds that of the majority of GRB samples.

Key words: gamma-rays: ISM – methods: numerical – radiation mechanisms: non-thermal

1. Introduction

Gamma-ray bursts (GRBs) represent the most energetic and brightest explosive events in the universe, occurring at cosmological distances. GRBs can be classified into two categories based on the duration of gamma-ray emission: long gamma-ray bursts (LGRBs), which have durations greater than 2 s, and short gamma-ray bursts (SGRBs), which have durations less than 2 s (Kouveliotou et al. 1993). Typically, LGRBs originate from the core-collapse of massive stars, whereas SGRBs arise from the merger of compact binary systems, such as neutron star–neutron star systems or neutron star–black hole systems (Eichler et al. 1989; Woosley 1993; Zhang & Mészáros 2004; Kumar & Zhang 2015). In the classical GRB fireball model, a central engine, formed by the collapse of a massive star or the merger of compact objects, launches a collimated and ultra-relativistic outflow (Paczynski 1986; Piran 1999; Racusin et al. 2009; Zhang et al. 2015). Within this outflow, dissipative processes result in an intense prompt gamma-ray emission lasting from seconds to

minutes (Rees & Meszaros 1992; Thompson 1994; Maxham & Zhang 2009; Hu et al. 2014). Furthermore, interactions between the outflow and the surrounding circumburst medium produce a long-lasting, broadband synchrotron radiation known as afterglow emission, persisting from days to months (Mészáros & Rees 1997; Sari & Mészáros 2000).

With the launch of GRB satellites equipped with rapid response capabilities, such as Swift (Gehrels et al. 2004) and Fermi (Meegan et al. 2009), an increasing number of GRB afterglows have been detected. These afterglows are identified through follow-up observations triggered by gamma-ray emissions. However, there are instances of “orphan afterglows,” where GRB afterglow radiation is detected without a corresponding prompt gamma-ray emission. This phenomenon can be attributed to two primary factors. First, GRB jets exhibit a high degree of collimation, making it challenging for GRB satellites to observe the prompt emission when the viewing angle exceeds the half-width angle of the jet core, a scenario

referred to as the “off-axis” case. However, during the afterglow phase, as the bulk Lorentz factor decreases, the radiation’s beaming angle widens, which enables the observation of afterglow radiation to become possible (Huang et al. 2002). Second, “dirty fireballs,” characterized by initial Lorentz factors much less than 100 due to significant baryon loading, can produce broadband afterglow radiation. However, the associated prompt emission is too weak for detection by GRB satellites (Paczynski 1998; Dermer et al. 1999). Consequently, in order to understand the properties of the whole GRB population well, it is essential to search and study the properties of the “orphan afterglows.”

Before the deployment of the Zwicky Transient Facility (ZTF; Bellm et al. 2018; Graham et al. 2019), only three optical afterglows had been observed which were not triggered by GRB prompt emission. In a retrospective survey, the Odyssey, INTEGRAL (SPI-ACS), and Konus missions identified GRB 140226A as the prompt emission counterpart to iPTF14yb (Hurley et al. 2014; Cenko et al. 2015), while POLAR, AstroSat, Konus-Wind, and INTEGRAL observed that GRB 170105A was the prompt emission counterpart of ATLAS17-aeu (Bhalerao et al. 2017; Svinikin et al. 2017). PTF11agg, the only optical transient source without a GRB counterpart (Wang & Dai 2013; Wu et al. 2014; Wang et al. 2015, 2016), was identified as likely being a “dirty fireball” by Cenko et al. (2013). The ZTF, characterized by its high-cadence, large field of view, and rapid follow-up capabilities, has enabled people to find more optical afterglow candidates (Dekany et al. 2020). From 2020 to 2022, ZTF detected twelve optical afterglow candidates, four of which (AT2020blt, AT2021any, AT21lfa, and AT2022cmc) did not exhibit corresponding GRB prompt emissions in retrospective searches. Regarding AT2020blt, Sarin et al. (2022) proposed that it might be interpreted as the on-axis afterglow of a long-duration GRB. Due to its low gamma-ray radiation efficiency, falling below 0.3%–4.5%, its prompt emission cannot be detected by current missions. The multi-band afterglow data fitting conducted by Xu et al. (2023) for AT2021any considered both the top-hat jet model and the structured Gaussian jet model. Their analysis revealed that the structured Gaussian jet model provided a better fit result, suggesting that AT2021any might be a “dirty fireball” observed on-axis. Furthermore, Andreoni et al. (2022) confirmed that AT2022cmc is a jetted tidal disruption event based on the characteristics of its X-ray, submillimeter, and radio light curves.

The light curve of AT2021lfa exhibits features consistent with those of GRB afterglows. However, the absence of corresponding prompt emissions suggests that it may be a potential candidate for an “orphan afterglow.” Lipunov et al. (2022) employed the smooth optical self-similar emission (SOSS) model for GRBs to model the optical light curve of AT2021lfa. The fitting results revealed an initial Lorentz factor of $\Gamma_0 = 20 \pm 10$. Consequently, they proposed that AT2021lfa

is most likely to be a “dirty fireball.” Ho et al. (2022) utilized a single power-law function to fit the light curves of the r , g , and i bands of AT2021lfa.

In this paper we re-investigate the properties of AT2021lfa by incorporating more observational data from radio, optical and X-ray bands, thereby imposing further constraints on the nature of AT2021lfa. Based on the empirical formula for the early-phase afterglow bump, we determine both the burst time and peak time of AT2021lfa. Employing the `afterglowpy` tool, we conduct a multi-band afterglow fitting analysis for AT2021lfa. Throughout the fitting process, we consider the temporal evolution of microphysical parameters ϵ_e , ϵ_B (the energy fraction given to electrons and magnetic field), and ξ_N (the fraction of accelerated electrons) which significantly improves our fitting results, particularly in the radio band. The fitting results strongly suggest that AT2021lfa is highly likely to be a “dirty fireball” with an initial Lorentz factor of approximately 18. In Section 2 we describe the multi-wavelength observation of AT2021lfa. The determination of AT2021lfa’s burst time and the multi-band light curve and spectra fitting are presented in Section 3. In Section 4, we discuss the property of AT2021lfa and compare its light curve features with those of GRB afterglows. Finally, we provide a summary of our findings and conclusions in Section 5.

2. Observations

AT2021lfa (ZTF21aayokph) was discovered by ZTF at the position R.A. (J2000): 12:32:48.725, decl. (J2000): $-01:29:22.56$. The optical transient was initially detected at 05:34:48 UTC on 2021 May 4, with a magnitude of $r = 18.60 \pm 0.08$, and at 07:30:09 UTC on 2021 May 4, with a magnitude of $g = 18.80 \pm 0.11$. The most recent upper limits were recorded on 2021 May 2, at 07:27:50 UTC (referred to as t_{up}), with $r > 20.23$ mag, and at 06:09:56 UTC with $g > 20.58$ mag (Yao et al. 2021b). The Liverpool Telescope (LT) (Steele et al. 2004) conducted rapid follow-up observations in the r filter and g filter at 15.5 and 19 hr after the first detection, revealing a rapid fading of AT2021lfa (1.9 mag day^{-1} in r -band) and colors ($g - r = 0.17 \pm 0.14$ mag) consistent with a non-thermal spectral energy distribution (SED). Considering the fast decay of flux and the reddened color, Yao et al. (2021b) suggested that AT2021lfa is a potential candidate for a GRB optical afterglow.

In the optical band, in addition to the observations by ZTF and LT, DDOTI (Watson et al. 2021), RATIR (Butler et al. 2021), NEXT (Fu et al. 2021), Assy (Kim et al. 2021), Lowell Discovery Telescope (O’Connor et al. 2021), Mondy and Koshka (Pankov et al. 2021), and LBT (Rossi et al. 2021) also conducted rapid follow-up photometric observations of AT2021lfa. Of particular significance, the MASTER-OAFA robotic telescope had observed AT2021lfa in survey mode three hours before the first detection by ZTF (Lipunov et al. 2021). MASTER captured the phase of steady brightening in

AT2021lfa, providing valuable insights for constraining the time of peak luminosity. Yao et al. (2021a) observed AT2021lfa with GMOS-S and identified $z = 1.063$ as the most probable redshift. Optical photometry has been corrected for Galactic extinction with $E(B - V) = 0.026$ mag (Schlafly & Finkbeiner 2011). The amount of extinction A_V of the host galaxy, obtained by fitting the SED of AT2021lfa with the SMC template extinction law (Li et al. 2008), is very small and can be neglected.

In the X-ray band, Swift/XRT observed AT2021lfa 1.0 day after the initial ZTF detection, with two separate epochs totaling an exposure time of 5 ks. X-ray emission from AT2021lfa was detected only in the first epoch. For observation data, we refer to Ho et al. (2022). Assuming the photon index $\Gamma_0 = 2$, we converted the observed flux in the 0.3–10 keV range to the flux density at 2 keV.

In the radio band, VLA observed AT2021lfa at nine different epochs. The observations spanned from a few days after the first ZTF observation to several hundred days later. We obtained the radio band data from Ho et al. (2022).

3. Method and Results

3.1. Fitting the Burst Time of AT2021lfa

Precisely determining the burst times (T_0) is imperative for investigating the fundamental physical mechanisms responsible for both the prompt gamma-ray emission and the afterglow radiation of GRBs. Traditionally, the burst time is determined by the trigger time observed from high energy satellites. However, in cases involving ‘‘orphan afterglow,’’ confirming the burst times presents a challenge. Ho et al. (2022) utilized a single power-law function to fit the light curves of the r , g , and i bands of AT2021lfa. This allowed them to estimate the burst time as $T_0 = 2021$ May 3, 06:57:36 (all dates and times provided in this article are in Coordinated Universal Time, UTC). In contrast, Lipunov et al. (2022) employed the SOSS model to match the light curve of AT2021lfa and derived a burst time: $T_{\text{orig}} = 2021$ May 4, 01:33. A discrepancy of 0.77 day is evident in the burst times obtained through these two approaches, which would significantly impact the subsequent analysis of light curve fitting for AT2021lfa.

To further determine the burst time of AT2021lfa, we consider an alternative method for estimating this parameter. In the framework of the GRB internal and external shock model, when the fireball reaches the deceleration radius, it undergoes a transition from the coasting phase to the deceleration phase. During the early afterglow phase, the jet interacts with the surrounding circumburst medium, leading to electron acceleration and then producing synchrotron radiation. Consequently, the afterglow light curve begins to rise. Once approximately half of the fireball’s energy is transferred to the circumburst medium, the light curve reaches its peak and subsequently enters a declining phase. As a result, the light curve would

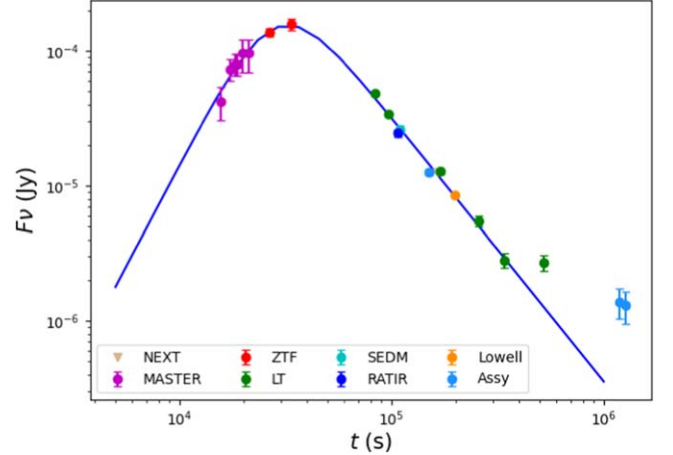


Figure 1. The light curve of AT2021lfa in r band. The solid line is the fitted result with the empirical formula proposed by Kocevski & Liang (2001).

exhibit a gradual bump during the initial afterglow phase. For AT2021lfa, a noticeable bump is observed. Kocevski & Liang (2001) introduced an empirical formula to model the early light curve bump of the afterglow

$$F(t) = F_p \left(\frac{t - dt}{t_{p1} - dt} \right)^r \left[\frac{d}{r + d} + \frac{r}{r + d} \left(\frac{t - dt}{t_{p1} - dt} \right)^{r+1} \right]^{\frac{r+d}{r+1}}, \quad (1)$$

where F_p represents the maximum observed flux during the peak time, and t_{p1} is defined as the time span between t_{up} and the peak time t_{peak} , calculated as $t_{p1} = t_{\text{peak}} - t_{\text{up}}$. The temporal gap from t_{up} to the burst time T_0 is denoted as dt , $dt = T_0 - t_{\text{up}}$. The parameter r represents the rising power-law index, while d signifies the decaying power-law index.

The magnitude of AT2021lfa, observed by the MASTER telescope, is calibrated by using reference stars within the G band from the Gaia Early Data Release 3 (EDR3), a wavelength range similar to that of the r band. Therefore, we approximate the observations in the G band as those in the r band. Furthermore, we convert the initial observational data from the ZTF g band to the r band by taking the spectral index as -1 (the spectral index of AT2021lfa was measured to be -1 at about 04:00 UTC on May 5). Subsequently, we employ emcee, a Python-based ensemble sampling technique for Markov Chain Monte Carlo, to fit the r -band light curve of AT2021lfa using Equation (1) by taking F_p , t_{p1} , dt , r , and d as free parameters.

The fitted light curve is displayed in Figure 1, while Figure 2 illustrates the posterior distribution of parameters. From Figure 1, it can be observed that after about 4×10^5 s, the light curve significantly flattens, possibly due to contributions from the host galaxy. Therefore, observational data beyond 4×10^5 s were not included in our fitting. The obtained parameters are as

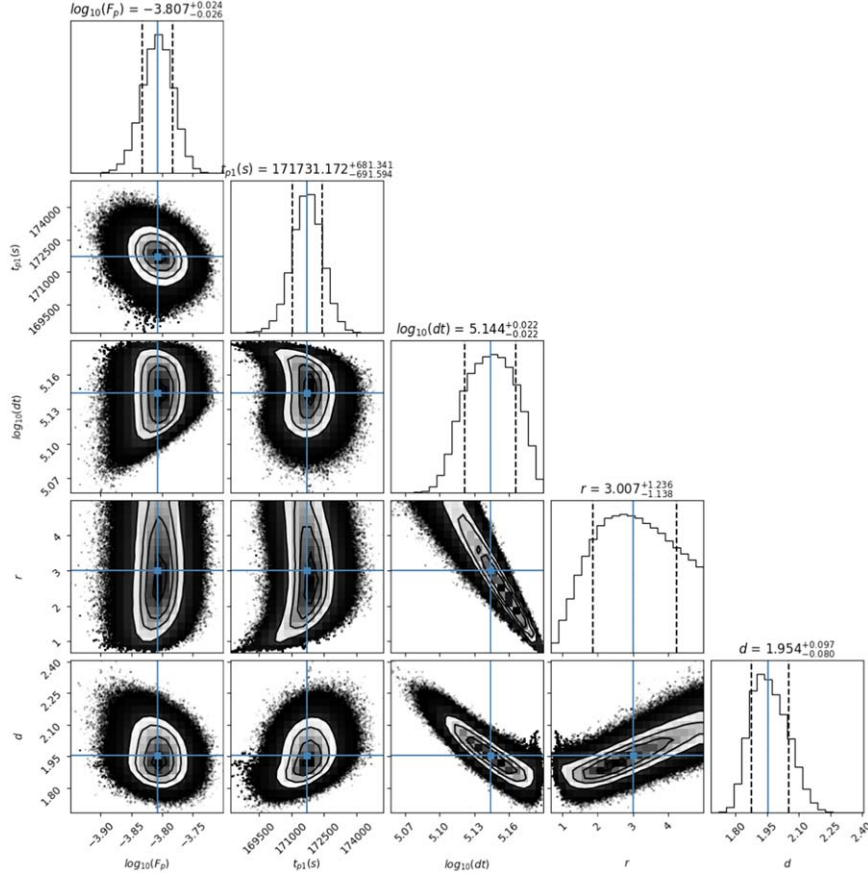


Figure 2. The posterior parameter distribution for AT2021lfa.

follows: the peak flux $F_p = (1.560^{+0.089}_{-0.091}) \times 10^{-4}$ Jy; the duration t_{p1} between the reference time t_{up} and the peak time t_{peak} is (171731^{+681}_{-692}) s; the time interval dt between the burst time T_0 and the reference time t_{up} is (139316^{+7239}_{-6882}) s; the rising power-law index $r = (3.007^{+1.236}_{-1.138})$; and the decaying power-law index $d = (1.954^{+0.097}_{-0.080})$. Therefore, the burst time is determined as $T_0 = 2021$ May 3, 22:09:50 $^{+02:00:39}_{-01:54:42}$, and the peak time is represented by $t_{peak} = 2021$ May 4, 07:10:01 $^{+00:11:21}_{-00:11:32}$. Comparing our results with those obtained by Lipunov et al. (2022), it is evident that our inferred burst time is earlier than theirs and meanwhile the peak time is somewhat later. The fitted rising power-law index, $r \sim 3$, is consistent with the rising index expected for the early afterglow light curves in a uniform medium (Panaitescu & Vestrand 2008).

3.2. Fitting of AT2021lfa Multi-band Afterglow

Afterglowpy is an open-source modeling tool designed for GRB afterglows. It enables simultaneous fitting of multi-band data in X-ray, optical, and radio frequencies (Cunningham et al. 2020; Ryan et al. 2020; Li et al. 2022). The tool employs the single-shell approximation to simulate the interaction

between GRB jets and a uniform external medium. Additionally, it utilizes a semi-analytical approach to calculate the synchrotron radiation generated by the forward shock. Afterglowpy incorporates not only the top-hat model but also the Gaussian jet model and the Power-Law jet model.

The fluxDensity function in afterglowpy incorporates ten independent physical parameters essential for better fitting of the afterglow light curve. These parameters include θ_v (viewing angle), E_0 (on-axis isotropic equivalent energy), θ_c (half-width of the jet core), θ_w (truncation angle of the jet’s “wing”), b (power for power-law structure), n (circumburst density), p (power-law index for electron distribution), ϵ_e (thermal energy fraction in electrons), ϵ_B (thermal energy fraction in the magnetic field), and ξ_N (fraction of accelerated electrons). We employ the emcee Python package, in combination with the fluxDensity function from afterglowpy to fit the afterglow light curve. We assume log-uniform prior distributions for E_0 , n , ϵ_e , and ϵ_B , with the remaining parameters assigned uniform prior distributions.

The standard afterglow model assumes that microphysical parameters, such as ϵ_e , ϵ_B , and ξ_N , remain constant throughout the entire afterglow evolution. However, studies have indicated

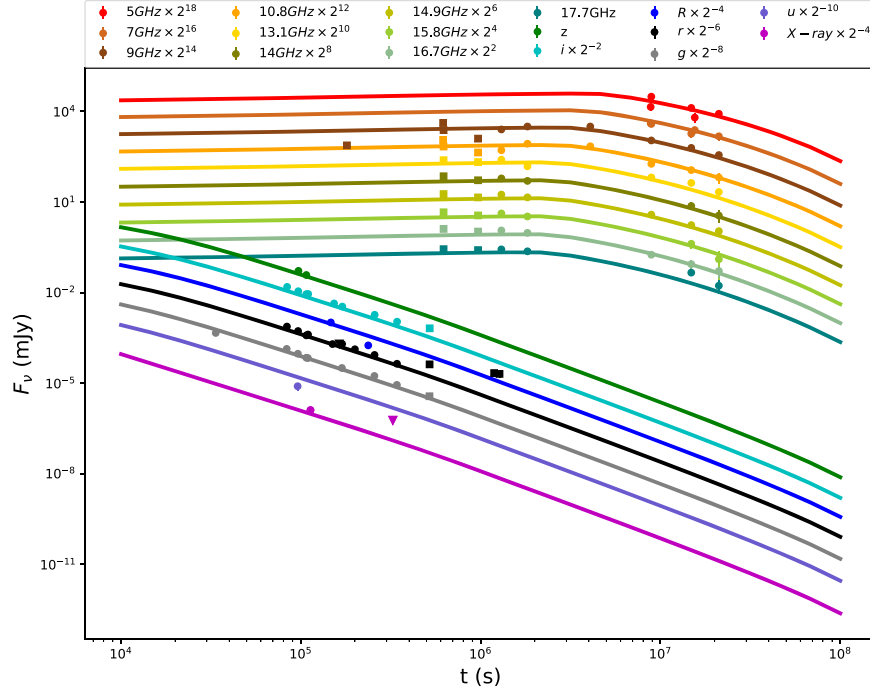


Figure 3. Multi-band afterglow data and fitting of AT2021lfa, where squares represent observed data points not utilized for fitting, and downward triangles denote upper limits.

that these parameters may vary with time during the course of the afterglow's evolution (Yost et al. 2003; Fan & Piran 2006; Ioka et al. 2006; Wei & Fan 2007). By fitting the early afterglows of several GRBs, it has been observed that the microphysical parameters ϵ_e and ϵ_B of the ultra-relativistic forward shock and mildly relativistic reverse shock are different (Fan et al. 2002; Kumar & Panaitescu 2003; Panaitescu & Kumar 2004; Wei et al. 2006), which suggests that these parameters may depend on the strength of the shock. To take into account the time-dependent variations of ϵ_e , ϵ_B , and ξ_N , our fitting procedure incorporates the assumption that these three physical parameters change over time following power-law behaviors: $\epsilon_e = \epsilon_{e0} t^{a_1}$, $\epsilon_B = \epsilon_{B0} t^{a_2}$, and $\xi_N = \xi_{N0} t^{a_3}$, where ϵ_{e0} , ϵ_{B0} , and ξ_{N0} represent the initial values of the respective parameters, while a_1 , a_2 , and a_3 signify the corresponding power-law exponents.

We employed `afterglowpy` to fit observational data in the radio, optical, and X-ray bands for AT2021lfa after the peak time. We considered three jet models for data fitting: top-hat, Gaussian, and Power-Law, respectively. As illustrated in Figure 3, the observed flux in the r and i bands exhibits a flattening trend beyond 4×10^5 s which may be the contribution from the host galaxy, thus we excluded this segment from the fitting process. It is worth noting that the intricate fluctuations observed in the radio band prior to 12 days may be attributed to interstellar scintillation (Rickett et al. 1984), therefore these radio data were excluded from the fitting analysis. The results of the

Table 1
The Results of Fitted Physical Parameters for AT2021lfa

Model	Top-hat	Gaussian	Power-law
θ_v [rad]	$0.526^{+0.181}_{-0.194}$	$0.521^{+0.181}_{-0.170}$	$0.530^{+0.173}_{-0.162}$
$\log_{10} E_0$	$54.774^{+0.433}_{-0.388}$	$54.928^{+0.404}_{-0.370}$	$54.848^{+0.406}_{-0.364}$
θ_c [rad]	$0.662^{+0.207}_{-0.235}$	$0.905^{+0.206}_{-0.273}$	$0.907^{+0.204}_{-0.243}$
θ_w [rad]	...	$0.697^{+0.212}_{-0.227}$	$0.687^{+0.208}_{-0.205}$
b	$5.055^{+3.374}_{-3.393}$
$\log_{10} n_0$	$1.039^{+0.697}_{-0.838}$	$1.139^{+0.812}_{-0.871}$	$1.041^{+0.760}_{-0.880}$
p	$3.092^{+0.034}_{-0.034}$	$3.091^{+0.035}_{-0.033}$	$3.085^{+0.035}_{-0.031}$
a_1	$-0.055^{+0.039}_{-0.069}$	$-0.060^{+0.042}_{-0.076}$	$-0.058^{+0.042}_{-0.074}$
$\log_{10} \epsilon_{e0}$	$-1.177^{+0.318}_{-0.329}$	$-1.170^{+0.295}_{-0.315}$	$-1.115^{+0.271}_{-0.287}$
a_2	$-0.355^{+0.081}_{-0.069}$	$-0.390^{+0.093}_{-0.067}$	$-0.382^{+0.094}_{-0.070}$
$\log_{10} \epsilon_{B0}$	$-4.465^{+0.702}_{-0.384}$	$-4.434^{+0.697}_{-0.407}$	$-4.402^{+0.739}_{-0.429}$
a_3	$-0.204^{+0.048}_{-0.051}$	$-0.220^{+0.054}_{-0.054}$	$-0.207^{+0.050}_{-0.056}$
ξ_{N0}	$0.695^{+0.218}_{-0.269}$	$0.729^{+0.174}_{-0.240}$	$0.728^{+0.170}_{-0.187}$

fitting procedure are summarized in Table 1. Remarkably, in both the Gaussian and Power-Law jet models, the half-width of the jet core exceeded the truncation angle of the jet, which indicates that the jet structure should be uniform. The physical parameters derived from modeling using the top-hat jet model are as follows: viewing angle $\theta_v = 0.526^{+0.181}_{-0.194}$ radians, isotropic equivalent energy $\log_{10} E_0 = 54.774^{+0.433}_{-0.388}$, half-width of the jet core $\theta_c = 0.662^{+0.207}_{-0.235}$ radians, power-law index for electron

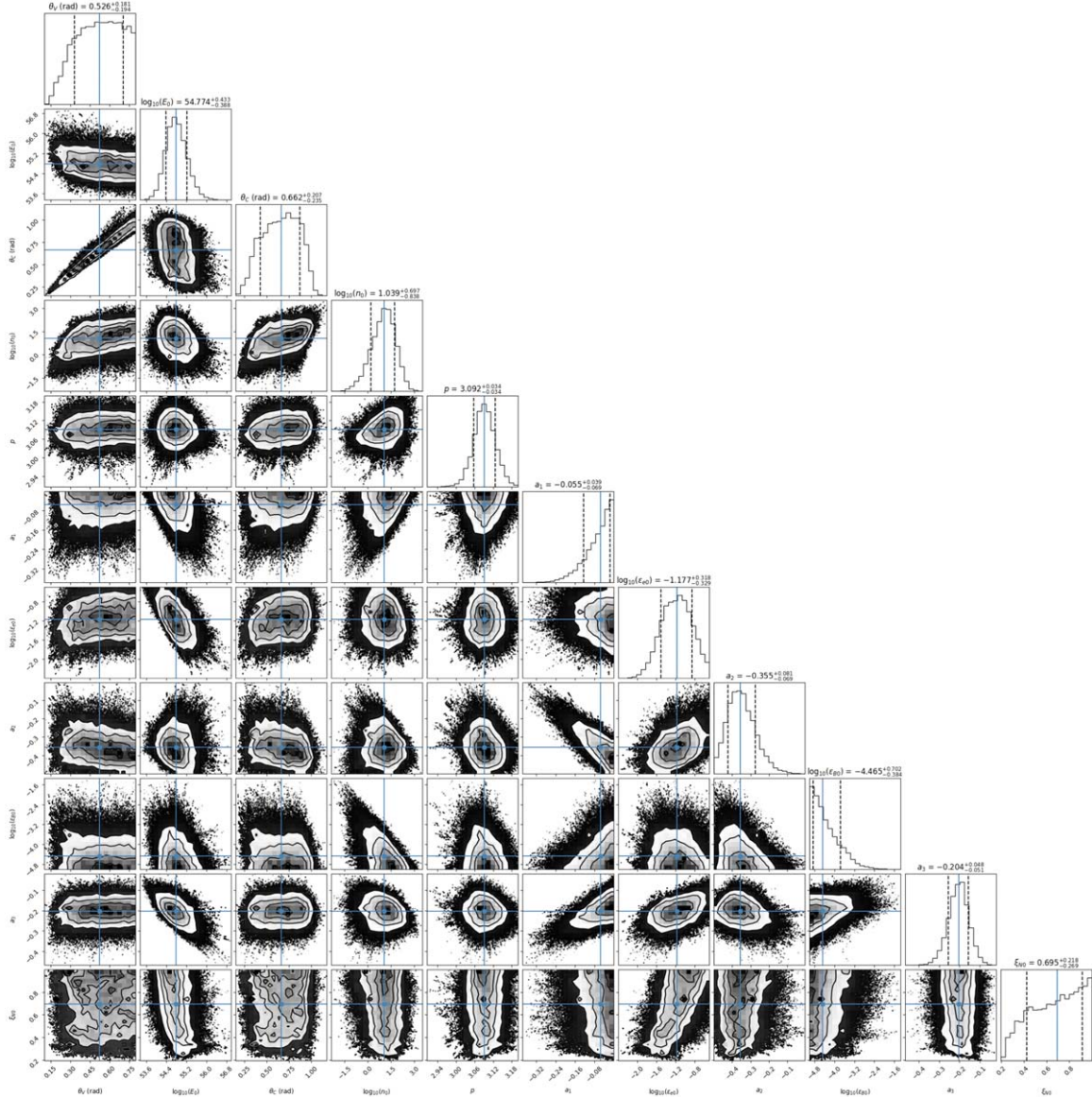


Figure 4. The posterior distribution of physical parameters of the top-hat jet model for AT2021lfa.

distribution $p = 3.092^{+0.034}_{-0.034}$, circumburst density $\log_{10} n_0 = 1.039^{+0.697}_{-0.838}$, the thermal energy fraction in electrons and the magnetic field are $\log_{10} \epsilon_{e0} = -1.177^{+0.318}_{-0.329}$ and $\log_{10} \epsilon_{B0} = -4.465^{+0.702}_{-0.384}$ respectively, the fraction of electrons that get accelerated $\xi_{N0} = 0.695^{+0.218}_{-0.269}$, and their corresponding temporal evolution indexes are $a_1 = -0.055^{+0.039}_{-0.069}$, $a_2 = -0.355^{+0.081}_{-0.069}$, $a_3 = -0.204^{+0.048}_{-0.051}$ respectively.

The multi-band light curve of AT2021lfa was successfully fitted using the physical parameters derived from the top-hat jet model, as presented in Figure 3. Notably, the u -band observations exhibit a lower trend compared to the fitted light curve, possibly due to Ly α absorption. Furthermore, Figure 4

illustrates the posterior distributions of the fitted parameters. Figure 5 illustrates the SED of AT2021lfa at 1.24 days. The SED was modeled using `afterglowpy`. It is evident from the figure that the SED exhibits a break at approximately 4×10^{18} Hz (the cooling frequency ν_c). Consequently, the optical and X-ray observations fall within the $\nu_m < \nu_{\text{opt}} < \nu_x < \nu_c$ region at 1.24 days.

4. Discussion

When a transient source exhibits similar light curve features to those of a GRB afterglow, but no associated prompt gamma-ray emission is detected, it is categorized as an “orphan

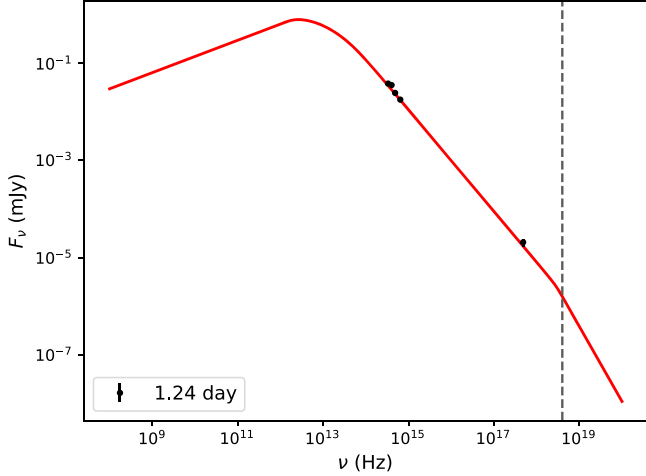


Figure 5. Observed SED of AT2021lfa (points) and the top-hat fit (red line) from afterglowpy at 1.24 days. The dotted line indicates the cooling frequency (ν_c).

afterglow.” The “orphan afterglow” phenomenon can be attributed to two potential factors. First, these events could arise from what are known as “dirty fireballs.” Second, they might result from off-axis observations, where the GRB jet is not directed toward Earth.

The Third Interplanetary Network (IPN3) comprises ten space satellites designed for continuous all-sky monitoring of GRBs. The most sensitive GRB satellites within IPN3 include the KONUS instrument on the Wind spacecraft, the Swift Burst Alert Telescope, and the Fermi Gamma-ray Burst Monitor. For AT2021lfa, Ho et al. (2022) performed a search within the IPN3 GRB observation archives to identify potential prompt emission counterparts. However, no corresponding prompt emission was detected. As a result, AT2021lfa has been classified as an “orphan afterglow” candidate. Based on KONUS-Wind observations, Ho et al. (2022) determined an upper limit for the isotropic prompt emission energy of AT2021lfa: $E_{\gamma, \text{iso}} < 1.2 \times 10^{51}$ erg. The isotropic kinetic energy of AT2021lfa, determined from the light curve fitting, is $E_{K, \text{iso}} = 5.943 \times 10^{54}$ erg. By applying the radiation efficiency formula $\eta = \frac{E_{\gamma, \text{iso}}}{E_{\gamma, \text{iso}} + E_{K, \text{iso}}}$, we deduce that the upper limit for the radiation efficiency of AT2021lfa is 0.02%. Typically, observed GRBs display radiation efficiencies ranging from 1% to 90%. However, the derived radiation efficiency for AT2021lfa falls significantly below this range, indicating a notably low efficiency. The exceptionally low radiation efficiency of AT2021lfa may have two possible explanations. First, it may be an off-axis GRB whose prompt emission is not directed toward the Earth, so the observed radiation efficiency is very low. Alternatively, AT2021lfa may be a “dirty fireball,” with its notably low radiation efficiency attributed to its low initial Lorentz factor.

In order to avoid the so-called “compactness problem” and efficiently generate prompt gamma-ray emissions, the standard fireball model requires an initial Lorentz factor exceeding 100. Nevertheless, the circumburst environment around GRBs, no matter from the gravitational collapse of massive stars or the merger of compact binary stars, may carry an abundance of baryons, resulting in a challenge known as baryon contamination. Under such circumstances, the abundance of baryons within the fireball will result in lower Lorentz factor known as a “dirty fireball.” While the prompt emission from “dirty fireballs” is faint and undetectable by GRB satellites, their multi-band afterglow remains observable, allowing us to directly detect their afterglow without relying on the prompt emission trigger. By utilizing relationships involving the Lorentz factor, peak timescale, interstellar medium, and isotropic equivalent kinetic energy of the jet (Nakar 2007), we can estimate the approximate value of the initial Lorentz factor as follows

$$\Gamma_0 \approx 40 \left(\frac{E_{K, \text{iso}, 50}}{n_{\text{ism}}} \right)^{\frac{1}{8}} \left(\frac{100(1+z)}{t_{\text{peak}} - T_0} \right)^{\frac{3}{8}}, \quad (2)$$

where $E_{K, \text{iso}, 50}$ represents the isotropic kinetic energy in units of 10^{50} erg, and z denotes the redshift. We have determined the burst time of AT2021lfa as $T_0 = 2021 \text{ May } 3, 22:09:50$ and the peak time as $t_{\text{peak}} = 2021 \text{ May } 4, 07:10:01$. By substituting the fitted model parameters $E_{K, \text{iso}, 50}$ and n into Equation (2), we can estimate AT2021lfa’s initial Lorentz factor as about 18. This is consistent with the $\Gamma_0 = 20 \pm 10$ derived by Lipunov et al. (2022), indicating that AT2021lfa may be a “dirty fireball,” and its low prompt emission efficiency may be attributed to its relatively small initial Lorentz factor. Additionally, the baryon loading of the fireball can be calculated using $E_{K, \text{iso}} = M\Gamma_0 c^2$. Based on the bulk Lorentz factor distribution of GRB samples, Ghirlanda et al. (2018) found that the typical value of baryon loading is distributed around $10^{-6} M_{\odot}$. However, the baryon loading of AT2021lfa is approximately $1.2 \times 10^{-5} M_{\odot}$, which is higher than the $10^{-6} M_{\odot}$ obtained by Ghirlanda et al. (2018). This further supports the possibility that AT2021lfa is a dirty fireball.

Observations indicate that the GRB jets exhibit high collimation instead of isotropy. The prompt emissions of GRBs are more readily detectable only when the viewing angle (θ_v) is smaller than the opening angle of the jet core (θ_c) due to relativistic beaming effects. Consequently, a substantial portion of the prompt gamma-ray radiation from GRBs cannot be detected due to relatively large viewing angles. However, during the afterglow phase, as the Lorentz factor decreases, the radiation’s beaming angle widens, which enables the observation of afterglow radiation to become possible even in the case of off-axis viewing. The study of off-axis afterglows assists in exploring the lateral structure of the jet (Ryan et al. 2015). Notably, GRB 170817A serves as an example of an off-axis

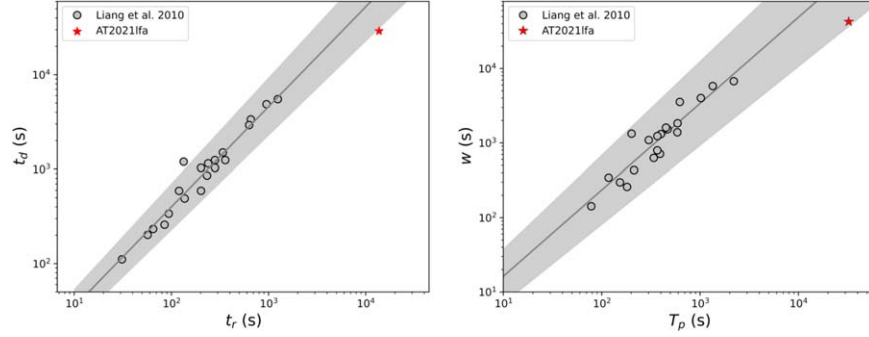


Figure 6. Correlations among timescales of GRB afterglow onset “bump.”

GRB, and multi-band afterglow light curve modeling suggests that its jet structure is more likely to be structured than uniform (Abbott et al. 2017; Alexander et al. 2018; Ghirlanda et al. 2019; Lamb et al. 2019). In contrast, fitting the multi-band afterglow data of AT2021lfa has revealed a viewing angle (θ_v) of 0.526 radians and a half-width of the jet core (θ_c) of 0.662 radians. Therefore, it can be deduced that AT2021lfa is observed on-axis.

In the early phase of the GRB afterglow, interpreting several observed phenomena poses a challenge for the conventional external shock model because of the intricate interactions between the external shockwave and the circumburst medium. While conducting X-ray early afterglow fitting, Yost et al. (2003), Ioka et al. (2006), Fan & Piran (2006) and Wei & Fan (2007) postulated that the microphysical parameters ϵ_e and ϵ_B of the shockwave exhibited temporal variation rather than constancy. Subsequently, they found a significant improvement in fitting results by taking into account the time-dependent nature of these microphysical parameters. During the analysis of multi-band data for AT2021lfa, it was observed that the late-time radio observations exhibit higher flux compared to the fitted light curve when keeping the microphysical parameters ϵ_e , ϵ_B , and ξ_N constant. To achieve a better fit to the observational data of AT2021lfa, we have taken into account the temporal variation of these three parameters, resulting in a significant improvement in fitting the late-time radio observations. The fitting results indicate a power-law decrease over time in the parameters ϵ_e , ϵ_B , and ξ_N , which may be attributed to the gradual weakening of the shock’s strength.

Since the launch of the Swift satellite, an increasing number of early-phase afterglows have been observed. A smooth bump has been detected within the early light curves of some afterglows (Liang et al. 2010; Han et al. 2022). Liang et al. (2010) conducted a statistical analysis of afterglow samples exhibiting this bump feature and found that these bump structures exhibit similarities, indicating a strong correlation among the timescales of these bumps. The relationships among

these timescales can be expressed as:

$$\log t_d = (0.48 \pm 0.13) + (1.06 \pm 0.06) \log t_r, \quad (3)$$

$$\log \omega = (0.05 \pm 0.27) + (1.16 \pm 0.10) \log t_p, \quad (4)$$

where ω represents the full width at half maximum (FWHM) of the bump, t_p denotes the time interval between the burst and the peak time, t_r is the rising timescale measured at the FWHM, and t_d is the declining timescale measured at the FWHM. Here we measure the characteristic timescales of the AT2021lfa bump to be: $\omega = 42,832$ s, $t_p = 32,413$ s, $t_r = 13,701$ s, and $t_d = 29,131$ s. We can compare the onset bump timescale of AT2021lfa with that of the afterglow samples from Liang et al. (2010), as depicted in Figure 6. The timescale of AT2021lfa adheres to the empirical timescale relationships obtained by Liang et al. (2010), but AT2021lfa’s bump displays a broader peak profile and a later peak time. This result is not surprising, as AT2021lfa is highly likely to be a “dirty fireball,” leading to prolonged deceleration timescales and delayed peak times.

Moreover, we conduct a comparison between the luminosity of AT2021lfa and the Swift GRB afterglows (Kann et al. 2011), as depicted in Figure 7. To facilitate this comparison, we transformed the Swift GRB afterglow in the observer frame to a common redshift of $z = 1$. The observed luminosity of AT2021lfa falls within the range of observations for the Swift afterglow sample. However, at approximately 1 day after the burst, AT2021lfa exhibits higher luminosity compared to the majority of Swift afterglow samples. This observation suggests that when searching for optical transient phenomena, ZTF prioritizes the detection of brighter sources. Consequently, studying faint optical afterglows requires the utilization of telescopes with higher sensitivity.

A comparison of the physical parameters of AT2020blt, AT2021any, and AT2021lfa is presented in Table 2. The fitting results indicate that AT2021lfa exhibits relatively large values for both the half-width of the jet core and the viewing angle. However, the observed GRBs generally display smaller half-widths of the jet core, along with smaller viewing angles. This trend could be attributed to observational selection effects.

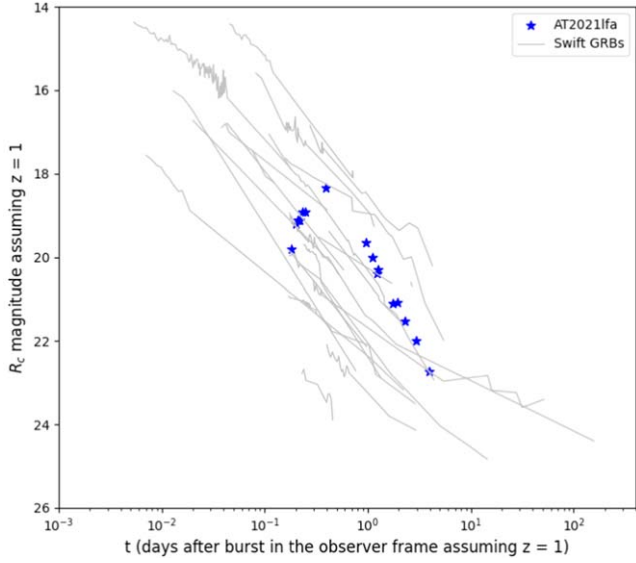


Figure 7. Compare the brightness of R_c band between AT2021lfa and Swift GRB samples.

Table 2

Comparison of AT2020blt, AT2021any, and AT2021lfa Physical Parameters

Transient	AT2020blt	AT2021any	AT2021any	AT2021lfa
θ_v [rad]	$0.06^{+0.05}_{-0.04}$	$0.55^{+0.27}_{-0.27}$	$0.02^{+0.003}_{-0.003}$	$0.526^{+0.181}_{-0.194}$
$\log_{10} E_0$	$53.61^{+0.25}_{-0.35}$	$52.58^{+0.03}_{-0.03}$	$52.99^{+0.15}_{-0.13}$	$54.774^{+0.433}_{-0.388}$
θ_c [rad]	$0.14^{+0.04}_{-0.04}$	$0.96^{+0.17}_{-0.28}$	$0.11^{+0.01}_{-0.01}$	$0.662^{+0.207}_{-0.235}$
θ_w [rad]	$0.05^{+0.02}_{-0.02}$...	$0.80^{+0.48}_{-0.46}$...
b	$5.14^{+2.89}_{-2.76}$
$\log_{10} n_0$	$1.90^{+1.30}_{-1.72}$	$0.06^{+0.19}_{-0.17}$	$-0.17^{+0.19}_{-0.19}$	$1.039^{+0.697}_{-0.838}$
p	$2.78^{+0.14}_{-0.20}$	$2.30^{+0.05}_{-0.05}$	$2.35^{+0.05}_{-0.06}$	$3.092^{+0.034}_{-0.034}$
$\log_{10} \epsilon_e$	$-1.10^{+0.34}_{-0.31}$	-1	$-0.88^{+0.07}_{-0.07}$	$-1.177^{+0.318}_{-0.329}$
$\log_{10} \epsilon_B$	$-1.64^{+0.73}_{-0.83}$	$-2.23^{+0.12}_{-0.13}$	$-3.23^{+0.16}_{-0.17}$	$-4.465^{+0.702}_{-0.384}$
ξ_N	$0.67^{+0.21}_{-0.26}$	1	1	$0.695^{+0.218}_{-0.269}$
References	Sarin et al. (2022)	Gupta et al. (2022)	Xu et al. (2023)	this work

Theoretically, scenarios should exist where both the half-width of the jet core and the viewing angle are relatively large (Gao & Dai 2010). Nevertheless, due to the nearly constant total energy released by the GRB central engine, an increase in the jet angle results in a decrease in the energy emitted per unit solid angle, which makes it more challenging to detect GRBs with larger jet angles. Our results indicate that AT2021lfa is one of the optical transient sources with relatively large jet core half-widths and viewing angles. Furthermore, Gupta et al. (2022) adopted the final upper limit detection time as the burst time and found unusually large values for both the jet core half-width and viewing angle of AT2021any. In a recent study, Xu et al. (2023) employed the burst time as a free parameter to derive the jet core half-width and viewing angle values for

AT2021any, as presented in Table 2. The derived jet core half-width and viewing angle values for AT2021any closely resemble those obtained for AT2020blt, which indicates that the value of burst time is very important for describing the afterglow behavior accurately.

5. Conclusions

AT2021lfa was detected by ZTF, followed by subsequent observations using Swift/XRT and ground-based telescopes. Notably, three hours before the initial ZTF observation, MASTER detected a gradual increase in the brightness of AT2021lfa. Due to its rapid flux decline in multiple wavelength bands, its reddish color ($g - r > 0$), and the absence of corresponding gamma-ray emission, AT2021lfa has been classified as a candidate for an “orphan afterglow.”

In our study, we applied the empirical formula introduced by Kocevski & Liang (2001) to fit the onset bump of AT2021lfa, resulting in a burst time of $T_0 = 2021 \text{ May } 3 \text{ 22:09:50}$ and a peak time of $t_{\text{peak}} = 2021 \text{ May } 4 \text{ 07:10:01}$. Notably, when comparing our results to those obtained by Lipunov et al. (2022), our derived burst time is earlier, and the peak time is somewhat later. Subsequently, we employed `afterglowpy` to fit the afterglow observations of AT2021lfa in the radio, optical, and X-ray bands after the peak time. During the fitting process, we considered power-law variations in microphysical parameters ϵ_e , ϵ_B , and ξ_N over time, resulting in a significant improvement in fitting the late radio band data. We determined the half-width of the jet core θ_c for AT2021lfa to be $0.662^{+0.207}_{-0.235}$ radians and the viewing angle θ_v to be $0.526^{+0.181}_{-0.194}$ radians, which does not support the possibility of off-axis observation for AT2021lfa and suggests that AT2021lfa may be an on-axis source with relatively large jet and viewing angles. By using the relationship between the peak time and the initial Lorentz factor, we estimated AT2021lfa’s initial Lorentz factor to be about 18, strongly suggesting that AT2021lfa is likely a “dirty fireball.” Because of its relatively low initial Lorentz factor, the prompt emission is comparatively weak, making it undetectable by gamma-ray satellites.

When comparing the initial bumps of AT2021lfa with the afterglow sample, we found that they exhibit similar structures, although AT2021lfa’s bump is broader and reaches its peak at a later time. Additionally, we noted that AT2021lfa’s brightness falls within the range of brightness observed in the Swift afterglow sample. However, at about 1 day after the burst, AT2021lfa’s brightness exceeds that of most Swift afterglow samples, suggesting a bias toward observing brighter optical transient sources by the ZTF. In order to detect GRBs with weaker prompt emissions and dimmer afterglows, more sensitive high-energy satellites and optical telescopes, such as Space Variable Objects Monitor (SVOM) and the Einstein Probe, are needed to make significant contributions in this research field.

Acknowledgments

We gratefully thank the anonymous referee for careful reading and many important suggestions that improved this paper. This work was supported by the National Natural Science Foundation of China (NSFC, grant Nos. 12073080, 11933010, 11921003, 12233011, and 12225305).

ORCID iDs

Yi-Ming Zhu  <https://orcid.org/0000-0002-9106-8718>

References

- Abbott, B. P., Abbott, R., Abbott, T. D., et al. 2017, *ApJL*, **848**, L13
- Alexander, K. D., Margutti, R., Blanchard, P. K., et al. 2018, *ApJL*, **863**, L18
- Andreoni, I., Coughlin, M. W., Perley, D. A., et al. 2022, *Natur*, **612**, 430
- Bellm, E. C., Kulkarni, S. R., Graham, M. J., et al. 2018, *PASP*, **131**, 018002
- Bhalerao, V., Kasliwal, M. M., Bhattacharya, D., et al. 2017, *ApJ*, **845**, 152
- Butler, N., Watson, A. M., Kuttyrev, A., et al. 2021, GCN, 29941, 1
- enko, S. B., Kulkarni, S. R., Horesh, A., et al. 2013, *ApJ*, **769**, 130
- enko, S. B., Urban, A. L., Perley, D. A., et al. 2015, *ApJL*, **803**, L24
- Cunningham, V., enko, S. B., Ryan, G., et al. 2020, *ApJ*, **904**, 166
- Dekany, R., Smith, R. M., Riddle, R., et al. 2020, *PASP*, **132**, 038001
- Dermer, C. D., Chiang, J., & Böttcher, M. 1999, *ApJ*, **513**, 656
- Eichler, D., Livio, M., Piran, T., & Schramm, D. N. 1989, *Natur*, **340**, 126
- Fan, Y., & Piran, T. 2006, *MNRAS*, **369**, 197
- Fan, Y.-Z., Dai, Z.-G., Huang, Y.-F., & Lu, T. 2002, *ChJAA*, **2**, 449
- Fu, S. Y., Zhu, Z. P., Liu, X., et al. 2021, GCN, 29948, 1
- Gao, Y., & Dai, Z.-G. 2010, *RAA*, **10**, 142
- Gehrels, N., Chincarini, G., Giommi, P., et al. 2004, *ApJ*, **611**, 1005
- Ghirlanda, G., Nappo, F., Ghisellini, G., et al. 2018, *A&A*, **609**, A112
- Ghirlanda, G., Salafia, O. S., Paragi, Z., et al. 2019, *Sci*, **363**, 968
- Graham, M. J., Kulkarni, S. R., Bellm, E. C., et al. 2019, *PASP*, **131**, 078001
- Gupta, R., Kumar, A., Pandey, S. B., et al. 2022, *JApA*, **43**, 11
- Han, S., Li, X., Jiang, L., et al. 2022, *Univ*, **8**, 248
- Ho, A. Y. Q., Perley, D. A., Yao, Y., et al. 2022, *ApJ*, **938**, 85
- Hu, Y.-D., Liang, E.-W., Xi, S.-Q., et al. 2014, *ApJ*, **789**, 145
- Huang, Y. F., Dai, Z. G., & Lu, T. 2002, *MNRAS*, **332**, 735
- Hurley, K., Golenetskii, S., Aptekar, R., et al. 2014, GCN, 15888, 1
- Ioka, K., Toma, K., Yamazaki, R., & Nakamura, T. 2006, *A&A*, **458**, 7
- Kann, D. A., Klose, S., Zhang, B., et al. 2011, *ApJ*, **734**, 96
- Kim, V., Pankov, N., Krugov, M., et al. 2021, GCN, 29950, 1
- Kocevski, D., & Liang, E. P. 2001, in AIP Conf. Ser. 586, 20th Texas Symp. on Relativistic Astrophysics, ed. J. C. Wheeler & H. Martel (Melville, NY: AIP), 623
- Kouveliotou, C., Meegan, C. A., Fishman, G. J., et al. 1993, *ApJL*, **413**, L101
- Kumar, P., & Panaitescu, A. 2003, *MNRAS*, **346**, 905
- Kumar, P., & Zhang, B. 2015, *PhR*, **561**, 1
- Lamb, G. P., Lyman, J. D., Levan, A. J., et al. 2019, *ApJL*, **870**, L15
- Li, A., Liang, S. L., Kann, D. A., et al. 2008, *ApJ*, **685**, 1046
- Li, X.-Y., He, H.-N., & Wei, D.-M. 2022, *RAA*, **22**, 085021
- Liang, E.-W., Yi, S.-X., Zhang, J., et al. 2010, *ApJ*, **725**, 2209
- Lipunov, V., Kornilov, V., Gorbvskoy, E., et al. 2021, GCN, 29959, 1
- Lipunov, V., Kornilov, V., Zhirkov, K., et al. 2022, *MNRAS*, **516**, 4980
- Maxham, A., & Zhang, B. 2009, *ApJ*, **707**, 1623
- Meegan, C., Lichti, G., Bhat, P. N., et al. 2009, *ApJ*, **702**, 791
- Mészáros, P., & Rees, M. J. 1997, *ApJ*, **476**, 232
- Nakar, E. 2007, *PhR*, **442**, 166
- O'Connor, B., Dichiara, S., Troja, E., et al. 2021, GCN, 29952, 1
- Paczynski, B. 1986, *ApJL*, **308**, L43
- Paczynski, B. 1998, *ApJL*, **494**, L145
- Panaitescu, A., & Kumar, P. 2004, *MNRAS*, **353**, 511
- Panaitescu, A., & Vestrand, W. T. 2008, *MNRAS*, **387**, 497
- Pankov, N., Belkin, S., Klunko, E., et al. 2021, GCN, 29954, 1
- Piran, T. 1999, *PhR*, **314**, 575
- Racusin, J. L., Liang, E. W., Burrows, D. N., et al. 2009, *ApJ*, **698**, 43
- Rees, M. J., & Meszaros, P. 1992, *MNRAS*, **258**, 41
- Rickett, B. J., Coles, W. A., & Bourgois, G. 1984, *A&A*, **134**, 390
- Rossi, A., Palazzi, E., Cusano, F. & Grawita Collaboration 2021, GCN, 30079, 1
- Ryan, G., van Eerten, H., MacFadyen, A., & Zhang, B.-B. 2015, *ApJ*, **799**, 3
- Ryan, G., van Eerten, H., Piro, L., & Troja, E. 2020, *ApJ*, **896**, 166
- Sari, R., & Mészáros, P. 2000, *ApJL*, **535**, L33
- Sarin, N., Hamburg, R., Burns, E., et al. 2022, *MNRAS*, **512**, 1391
- Schlafly, E. F., & Finkbeiner, D. P. 2011, *ApJ*, **737**, 103
- Steele, I. A., Smith, R. J., Rees, P. C., et al. 2004, *Proc. SPIE*, **5489**, 679
- Svinkin, D., Golenetskii, S., Aptekar, R., et al. 2017, GCN, 20406, 1
- Thompson, C. 1994, *MNRAS*, **270**, 480
- Wang, L.-J., & Dai, Z.-G. 2013, *ApJL*, **774**, L33
- Wang, L.-J., Dai, Z.-G., Liu, L.-D., & Wu, X.-F. 2016, *ApJ*, **823**, 15
- Wang, L.-J., Dai, Z.-G., & Yu, Y.-W. 2015, *ApJ*, **800**, 79
- Watson, A. M., Butler, N., Becerra, R. L., et al. 2021, GCN, 29940, 1
- Wei, D.-M., & Fan, Y.-Z. 2007, *ChJAA*, **7**, 509
- Wei, D. M., Yan, T., & Fan, Y. Z. 2006, *ApJL*, **636**, L69
- Woolsey, S. E. 1993, *ApJ*, **405**, 273
- Wu, X.-F., Gao, H., Ding, X., et al. 2014, *ApJL*, **781**, L10
- Xu, F., Huang, Y.-F., & Geng, J.-J. 2023, *A&A*, **679**, A103
- Yao, Y., Ho, A., & Perley, D. 2021a, TNSAN, 145, 1
- Yao, Y., Perley, D., & Ho, A. 2021b, GCN, 29938, 1
- Yost, S. A., Harrison, F. A., Sari, R., & Frail, D. A. 2003, *ApJ*, **597**, 459
- Zhang, B., & Mészáros, P. 2004, *IJMPA*, **19**, 2385
- Zhang, B.-B., van Eerten, H., Burrows, D. N., et al. 2015, *ApJ*, **806**, 15